

Supporting information

Highly efficient thermophones based on freestanding single-walled carbon nanotube films

Stepan A. Romanov^{1}, Ali E. Aliev², Boris V. Fine^{1,3}, Anton S. Anisimov⁴, Albert G. Nasibulin^{1,5*}*

¹ Skolkovo Institute of Science and Technology, Nobel Str.3, Moscow 121205, Russia

² Alan G. MacDiarmid NanoTech Institute, University of Texas at Dallas, Richardson, TX,
75083, USA.

³ Institute for Theoretical Physics, University of Heidelberg, Philosophenweg 19, 6912
Heidelberg, Germany

⁴ Canatu Ltd., Konalankuja 5, 00390, Helsinki, Finland

⁵ Department of Applied Physics, Aalto University, Puumiehenkuja 2, FI-00076 Espoo, Finland

KEYWORDS: Thermoacoustics, carbon nanotube, heat capacity per unit area, ultrasound

Contents:

S1 Experimental part..... 3

 S1.1 Areal density and iron concentration measurements 3

 S1.2 Purification by annealing in vacuum 4

 S1.3 Methods and description of experiments 5

S2 Theoretical part..... 7

 S2.1 Temperature oscillations 8

 S2.2 Density and velocity oscillations near the sample surface..... 10

 S2.3 Pressure oscillations near the sample surface 12

 S2.4 Flat transducers 13

 S2.5 Directivity gain of a flat transducer 14

 S2.6 COMSOL modeling..... 16

References:..... 17

S1 Experimental part

S1.1 Areal density and iron concentration measurements

To measure the areal density, ρ_a , and iron concentration in the single-walled carbon nanotube (SWCNT) films we collected a thick film with the size of $21.0 \times 29.7 \text{ cm}^2$ and 50% of optical transmittance (Figure S1a). The film (Figure S1b) was crumpled up and placed in the Al_2O_3 crucible. The film total mass of 3.47 mg was measured by thermal analyzer (NETZSCH STA 449F3). After SWCNTs were heated to $1400 \text{ }^\circ\text{C}$ in the air atmosphere, the mass of 0.84 mg was measured for the remaining Fe_2O_3 (Figure S1c).



Figure S1. Photographs of a) a thick SWCNT film with 50% of optical transmittance collected on an A4 size filter, b) a crumpled up thick SWCNT film. c) remaining Fe_2O_3 in the Al_2O_3 crucible after the sample treatment to $1400 \text{ }^\circ\text{C}$.

Therefore, the weight concentration of iron in our films can be calculated to be about 16.94 % and the areal density of the film with the 50% transmittance, $\rho_{a_{0.5}}$, is equal to $5.5 \mu\text{g}/\text{cm}^2$, while the areal density for the film with arbitrary transmittance can be defined as:

$$\rho_a = \rho_{a_{0.5}} \frac{\log_{10}(\xi)}{\log_{10}(0.5)}, \quad (\text{S1})$$

where ξ is the film optical transmittance at 550 nm.

S1.2 Purification by annealing in vacuum

Purification of SWCNT films was performed in a vacuum chamber (less than 10^{-4} Torr) with a Joule heating by applying 6 – 20 W/cm² (varied depending on the sample thickness) of the electric power with a direct current, until the samples start to glow brightly (Figure S2).

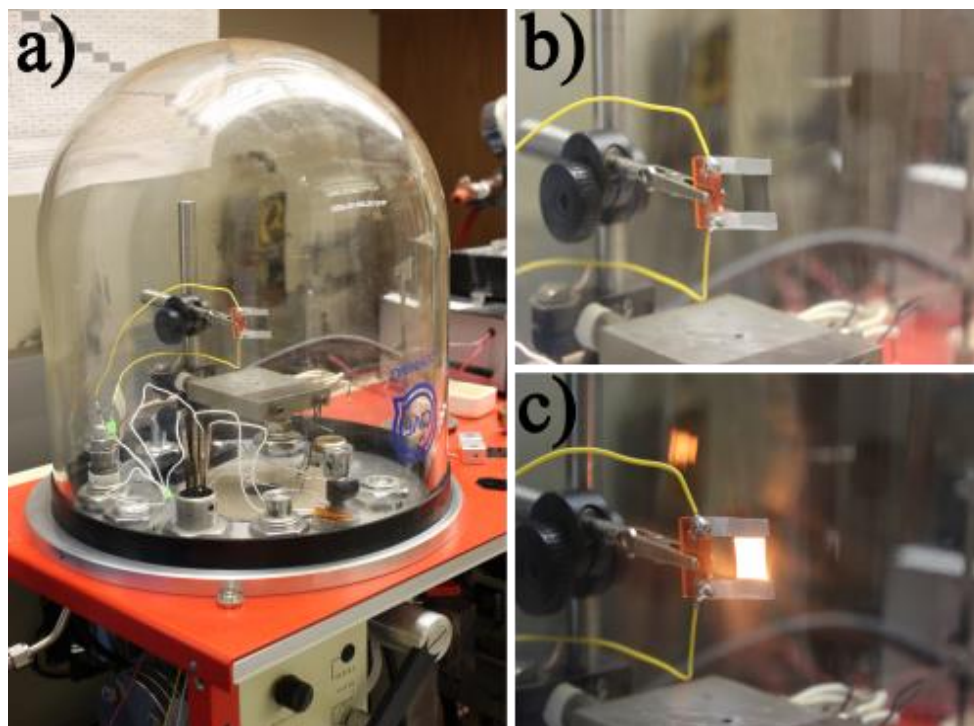


Figure S2. Photographs of a) a vacuum chamber. b) SWCNT-60% sample placed in the vacuum chamber. c) the SWCNT-60% under Joule heating at 25 W/cm² of applied power.

To prove iron particle evaporation from the films of SWCNTs we carried out transmission electron microscopy observation of the samples before and after purification by vacuum annealing (Fig. S3).

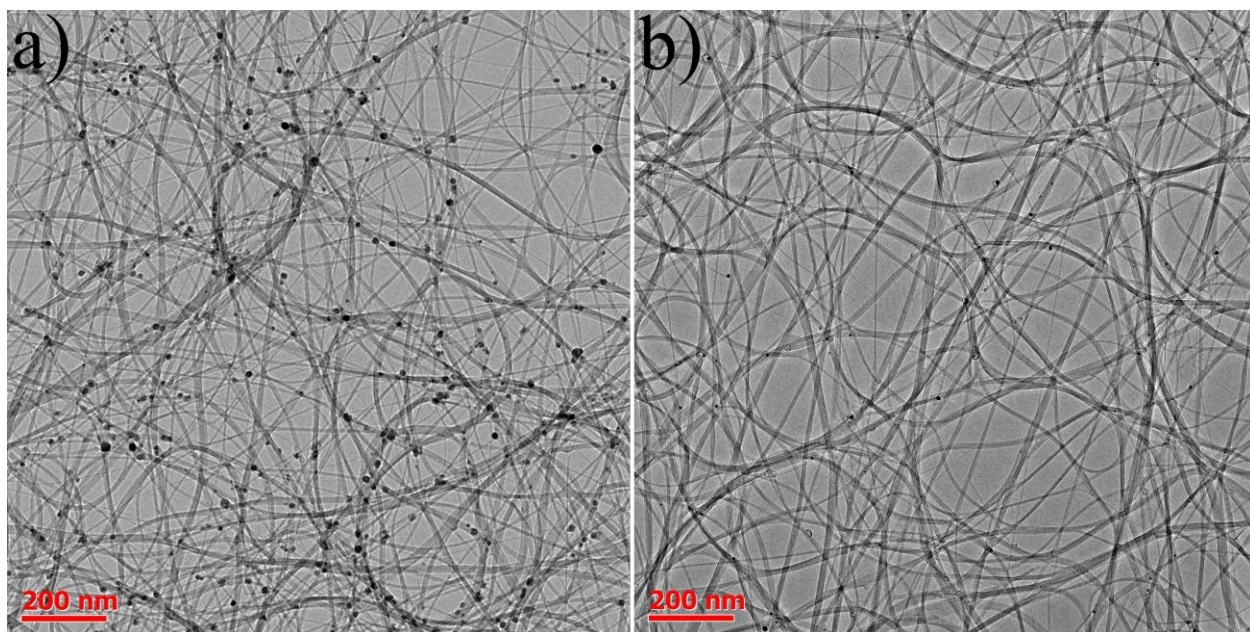


Figure S3. Typical TEM images of SWCNT films of 90% transmittance a) before and b) after vacuum annealing.

S1.3 Methods and description of experiments

The experimental setup consisted of two parts: sound generation and its detection (see Figure 2c in the main text). Both parts were controlled via Hewlett-Packard Interface Bus (GPIB) by a laptop with software written in the python programming language. In the experiments, the program made a frequency sweep of the current from 0.5 kHz to 50.5 kHz with step of 1 kHz. The electric input power was adjusted to obtain $\sim 80^{\circ}\text{C}$ of average temperature on the surface of the sample, where the temperature was monitored with FLIR T650-sc. For a certain frequency from the frequency range the generation process was the following: 1) sine wave was generated by a generator (Keysight Agilent 33250A); 2) the wave was amplified by an amplifier (TREK PZD350A M/S); 3) the sine signal reached the sample, induced Joule heating and, consequently, sound propagation, while the oscilloscope (Tektronix DPO4104B-L) controlled the signal shape; 4) a multimeter (Keithley 2000) measured the voltage on the sample, while another multimeter

(Keithley 2000) measured current through the sample by measuring the voltage drop across a series-connected high power 1 Ohm resistor. The detection process was following: 1) the signal was received with a microphone (B&K 4138-A-015) (free-fields corrections were taken into account) and amplified with a low-noise preamplifier (Stanford research systems SR 560), which also filtered undesirable low and high frequencies; 2) the second harmonic of the original signal was measured with a lock-in amplifier (Stanford research systems SR 830), which parameters were controlled by the program for optimal measurements. The transmittance of the samples was measured with a UV-vis-NIR spectrophotometer (Lambda 1050).

S2 Theoretical part

The sound pressure for the point source case when the sound wavelengths much larger than the thermophone size was obtained in Ref. 1. It is extended here for the case of a source of finite size in comparison to the sound wavelength. For instance, in the samples with the size of $1 \times 1 \text{ cm}^2$ the frequency of the transition from large to small wavelengths is 16 kHz.

The thermal and acoustic parts of the problem can be solved separately at low frequencies $f \ll v_s^2/\alpha_T$, where f is the frequency of the sound, v_s is the speed of sound, α_T is the thermal diffusivity¹. The logical sequence of our theory derivation is presented in Figure S4. Briefly, the oscillation in time heating results in the oscillating air pressure at the surface of the sample, which then becomes converted into the propagating sound waves. One then needs to take into account the diffraction effects to obtain the measured sound pressure.

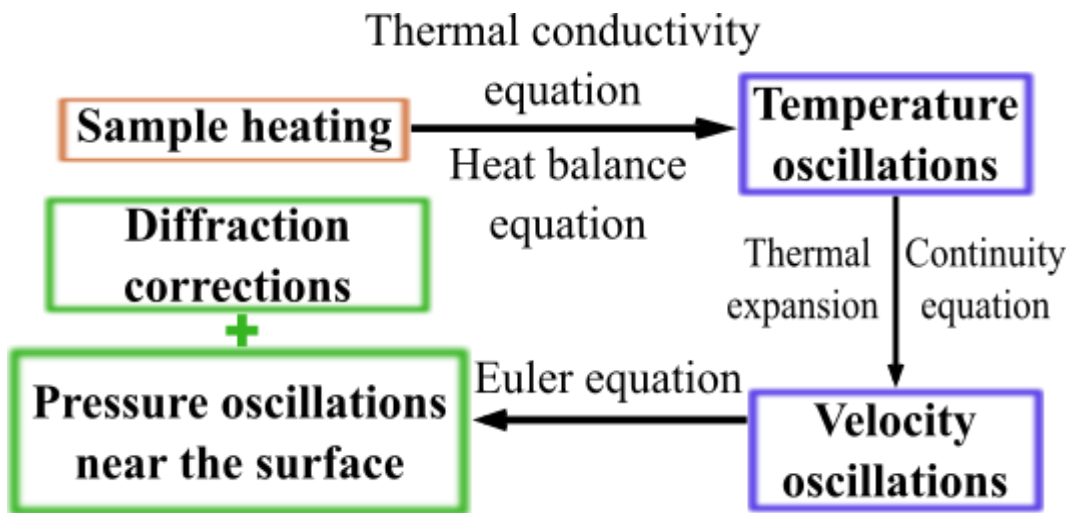


Figure S4. Diagram showing the principal steps in thermoacoustic theory derivation.

S2.1 Temperature oscillations

In thermophones, temperature oscillations in time lead to a sound propagation. In order to find an amplitude of the temperature oscillations, T_{osc} , we consider an electrically conducting sample of thickness, $2h$, and surface area, S . The sample is surrounded by air (Figure S5). When an alternating current with a frequency of $f/2$ passes through the sample, it causes oscillations in the power converted into the Joules heating of the sample:

$$P(t) = 2P_0 \sin^2(\pi f t) = P_0 - P_0 \cos(2\pi f t), \quad (S2)$$

where P_0 is the time average electrical input power. The first (time independent) term in Eq. S2, P_0 , induces Joule heating, which increases the temperature of the sample from the air temperature T_0 to higher value T_{avg} . The second (time dependent) term in Eq. S2 oscillating part of electrical power, $P_0 \cos(2\pi f t)$, leads to periodic temperature oscillations with an amplitude T_{osc} , which we determine below (see Movie).

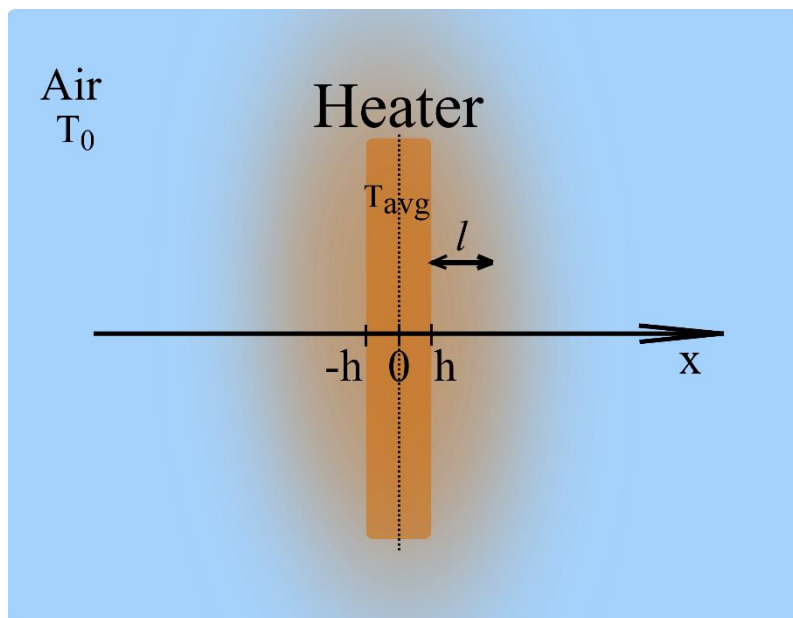


Figure S5. Heating illustration of the sample with a thickness of $2h$, which is placed in air.

To find T_{osc} , we consider the thermal conductivity equation

$$\rho_g C_g \frac{\partial \delta T(t, x)}{\partial t} = \kappa \Delta \delta T(t, x), \quad (\text{S3})$$

where t is a time, x is the axis of the coordinate in the direction perpendicular to the sample surface, ρ_g is the air density, C_g is the heat capacity of air per unit mass, and κ is the thermal conductivity of air.

We look for the solution of the form

$$\delta T(t, x) = T_{osc} e^{i(q(x-h) - \omega t)}, \quad (\text{S4})$$

where q is the wave number, $\omega = 2\pi f$ is the angular frequency. Substituting Eq. S4 into Eq. S3

we obtain $q = -\frac{(1-i)}{\sqrt{2}} \sqrt{\frac{\omega \rho_g C_g}{\kappa}}$. We also define the thermal diffusion length

$$l(\omega) \equiv \frac{1}{\text{Im } q} = \sqrt{\frac{2\kappa}{\omega \rho_g C_g}}. \quad (\text{S5})$$

The amplitude of temperature oscillations can now be found from the heat balance equation

$$\frac{P(t)}{S} = C_h \frac{\partial T(t, x)}{\partial t} - \kappa \frac{\partial T(t, x)}{\partial x} \quad (\text{S6})$$

where C_h is the heat capacity of the sample per unit area. It is defined as $C_h = \rho_h h C$, where ρ_h is the density of the sample, and C is the heat capacity of the sample per unit mass. Eq. S5 neglects the effects of convection, black body radiation and heat conduction to the electrical contacts.

Substituting Eq. S4 into Eq. S6 we obtain

$$T_{osc} = \frac{iP_0}{S(q\kappa + \omega C_h)}. \quad (\text{S7})$$

In order to verify Eq. S7 and approximations used above, we arranged numerical calculations in COMSOL software. The thermal conductivity equation of the used numerical model took into account convection effect introduced in heat flux module of COMSOL by condition of natural convection on a vertical wall. The results of the calculations of temperature amplitude, T_{osc} , with COMSOL and Eq. S7 for different values of the heat capacity per unit area found to be in a very good agreement, which prove the applicability of the approximations used in derivation of Eq. S7 (Figure S6).

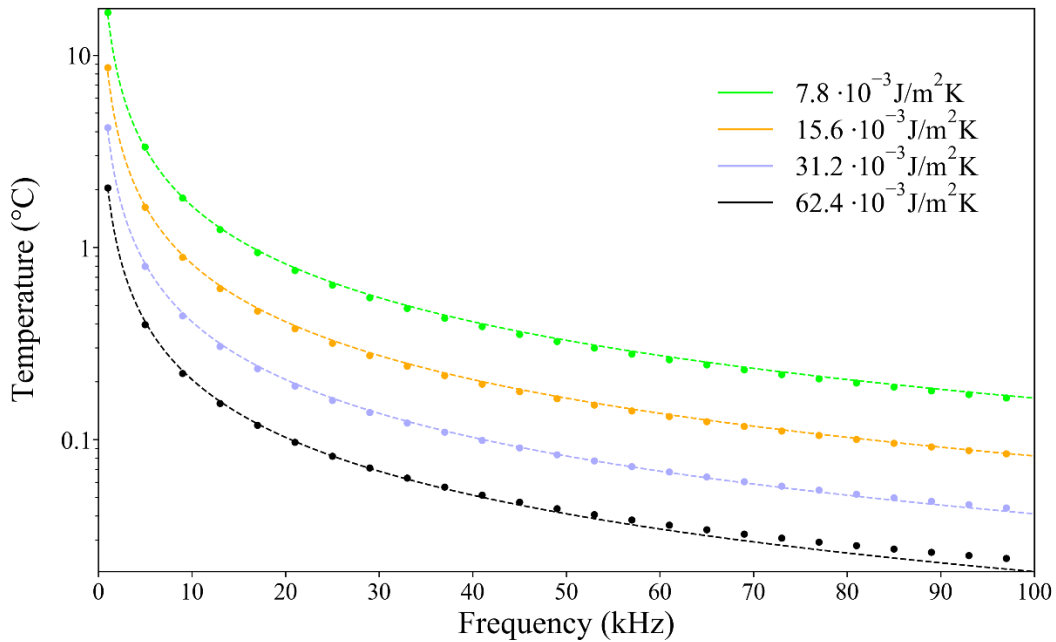


Figure S6. Dependence of temperature amplitude on the applied alternating current frequency for films of different heat capacity per unit area. The dashed lines correspond to Eq. S7., while the dots were calculated using COMSOL software by a finite element method.

S2.2 Density and velocity oscillations near the sample surface

The oscillations of air temperature near the surface of the sample lead to the oscillations of pressure p , and density ρ , within a layer of characteristic length $l(\omega)$. In general, the density

variation ρ , caused by changes in pressure δp , and temperature δT , can be expressed in the linear approximation as:

$$\delta\rho = \rho_g(\beta\delta p - \alpha\delta T), \quad (\text{S8})$$

where α is the thermal expansion coefficient, β is the compressibility. The latter two are defined as $\alpha \equiv -\frac{1}{\rho_g}\left(\frac{\partial\rho_g}{\partial T}\right)_p$ and $\beta \equiv \frac{1}{\rho_g}\left(\frac{\partial\rho_g}{\partial p}\right)_T$. Since, for the ideal gas, $p = \rho RT$, Eq. S8 takes the

form

$$\delta\rho = \rho_g\left(\frac{\delta p}{p_0} - \frac{\delta T}{T_{avg}}\right). \quad (\text{S9})$$

In Eq. S8 the term, $\delta p/p_0$, can be neglected, because it is several orders of magnitude smaller than $\delta T/T_{avg}$. The reason for this smallness is that the pressure adjusts to the change of external conditions ballistically with characteristic time l/v_s , while temperature adjusts diffusively on a much slower timescale $1/\omega$. This smallness is also the subject to the final consistency check after the amplitude of the pressure oscillations is obtained. Eq. S9 then translates into the following time dependent relation for the density oscillations

$$\delta\rho(t, x) = -\rho_g\left(\frac{\delta T(t, x)}{T_{avg}}\right). \quad (\text{S10})$$

The above density oscillations can now be converted into the oscillations of the gas velocity field $u(t, x)$. The velocity oscillations can be obtained with the help of the continuity equation

$$\frac{\partial\rho}{\partial t} = -\rho_g\frac{\partial u}{\partial x}. \quad (\text{S11})$$

The substitution of Eq. S10 and Eq. S7 into Eq. S11 then gives

$$\frac{\partial u}{\partial x} = \frac{-i\omega\rho_g\delta T(t, x)}{T_{avg}}. \quad (\text{S12})$$

Integrating Eq. 12 with respect to x , we obtain the asymptotic value of the amplitude of air velocity oscillations outside of the diffusive heating layer near the surface

$$u_0 = \frac{-i\omega}{T_{avg}} \int_h^\infty \delta T(t, x) dx = \frac{\omega T_{osc}}{q T_{avg}}, \quad (\text{S13})$$

where the origin of the x -axis is defined in Figure S5.

S2.3 Pressure oscillations near the sample surface

The sound pressure can now be found from the velocity field using the Euler equation for a compressible fluid without dissipation:

$$\frac{\partial u}{\partial t} + (u\nabla)u = -\frac{1}{\rho_g} \nabla p. \quad (\text{S14})$$

Let us now consider a solution of the Euler equation in a semi-open spherical geometry, namely, outside of the spherical boundary of radius a . For small variations of the density and pressure, and for $\ll v_s$, the boundary condition on the spherical surface is

$$\left. \frac{du}{dt} \right|_{r=a} = -\left. \frac{1}{\rho_g} \frac{dp}{dr} \right|_{r=a}. \quad (\text{S15})$$

We look for the solution of the form

$$p = A \frac{e^{i(kr-\omega t)}}{r}, \quad (\text{S16})$$

where r is the distance from the center of the sphere ($r \geq a$) and A is a constant. In Eq. 16 in order to simplify subsequent notations, we switch from δp to p to represent small deviation from the equilibrium pressure p_0 .

Substituting $\left. \frac{du}{dt} \right|_{r=a} = i\omega u_0$ and Eq. 16 into Eq. 15, we obtain

$$-i\omega u_0 = \frac{A}{\rho_g} \left(\frac{ika-1}{a^2} \right), \quad (\text{S17})$$

which in turn gives

$$|A| = \frac{\omega u_0 \rho_g a^2}{\sqrt{(ka)^2 + 1}}. \quad (\text{S18})$$

Eq. S18 applies to both small ($ka \ll 1$) and large ($ka \gg 1$) thermophones. After the velocity field from Eq. S13 and $k = 2\pi f/v_s$ are substituted in Eq. S18 and the result is further substituted in Eq. 16, we obtain the root-mean squared sound pressure of a spherical transducer.

$$p_{rms}(f, r) = \frac{f P_0}{2\sqrt{2} C_g T_0 r} \frac{1}{\sqrt{\left(\frac{2\pi a f}{v_s}\right)^2 + 1}} \frac{1}{\sqrt{2\chi^2(f) + 2\chi(f) + 1}}, \quad (\text{S19})$$

where $\chi(f) = \frac{h\rho_h C_h}{l(2\pi f)\rho_g C_g}$. Here $l(2\pi f)$ is the function of frequency defined by Eq. S5.

S2.4 Flat transducers

The result for the spherical transducer given by Eq. S19 can now help us to obtain the sound pressure for a flat transducer of an arbitrary shape. In general, there are three regimes of the flat-transducer operation, which depend on the ratio between the sound wavelength and the characteristic sample size: (i) the regime of a point source when the wavelength much larger than the sample size, (ii) the regime of a large source when the wavelength much smaller than the sample size and (iii) the intermediate regime of finite source when the wavelength comparable with the sample size.

For a point source the result for the spherical transducer given by Eq. S19 applies entirely, using effective radius

$$a = \sqrt{S/4\pi}, \quad (\text{S20})$$

where S is the double-sided surface area of the flat transducer.

For a large source the isotropic spherical pressure front, given by Eq. S19, must be modified to account for the directivity of the sound emission as described below. However, in this case, the value of the pressure for the spherical transducer near the spherical surface, $p_{rms}(f, a)$ can still be used to obtain the pressure of the flat transducer near the flat surface again with the effective radius given by Eq. S20.

In the intermediate regime, strictly speaking, one needs to perform the complete numerical simulation of the coupled thermoacoustic equations, and we have indeed done this using COMSOL software as described below. However, we have found that, at least for the transducers of square shape, the intermediate regime is very well described by the preceding prescription for large transducers in combination with the directivity gain calculation described below.

S2.5 Directivity gain of a flat transducer

Directivity gain function is the ratio of intensity in a certain direction to the isotropically averaged intensity

$$G(r, \varphi, \theta) = \frac{I(r, \varphi, \theta)}{\frac{1}{4\pi} \int_0^{2\pi} \int_0^\pi I(r, \varphi', \theta') \sin \theta' d\varphi' d\theta'}, \quad (\text{S21})$$

where $I(r, \varphi, \theta)$ is the sound intensity, φ and θ are the azimuth and polar angles. The intensity distribution on the sphere of radius, r , surround the sample is proportional to the square of the sound pressure $p^2(r, \varphi, \theta)$.

In order to find $p(r, \varphi, \theta)$ we used Huygens-Fresnel principle, i.e. each point on the transducers surface was assumed to be a point source of spherical waves, $p_i = A_i \frac{e^{-ikr_i}}{r_i}$ (Fig. S7). The intensity of this point sources was chosen using the result for the spherical transducer and Eq. S19 as described in the preceding section. The results for the directivity gain calculation in front of the sample is presented in Fig. S8.

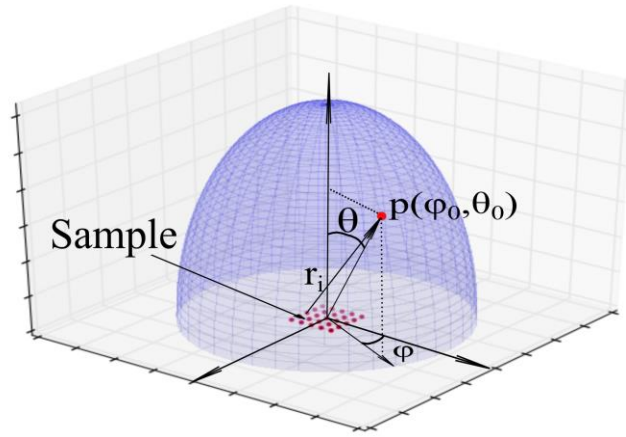


Figure S7. Spherical surface used for calculation of the directivity gain function.

The calculation of directivity gain of Eq. S21 by Huygens-Fresnel principle includes the transition from the near to the far field with an increase of the sphere radius. In order to verify these numerical results we compared them with the analytical result for the directivity of a square emitter in the far field:

$$D(\varphi, \theta) = \text{sinc}\left(\frac{k \sin \theta \cos \varphi L}{2}\right) \text{sinc}\left(\frac{k \sin \theta \sin \varphi L}{2}\right), \quad (\text{S22})$$

where $\text{sinc}(x) \equiv \frac{\sin(x)}{x}$, L is the edge lengths of the square transducer. The directivity is then calculated as:

$$G(r, \varphi, \theta) = \frac{D^2(\varphi, \theta)}{\frac{1}{4\pi} \int_0^{2\pi} \int_0^\pi D^2(\varphi', \theta') \sin \theta' d\varphi' d\theta'} \quad (\text{S23})$$

As seen in Fig. S8 the analytical result of Eq. 23 is in excellent agreement with the numerical calculation for large distances from the source.

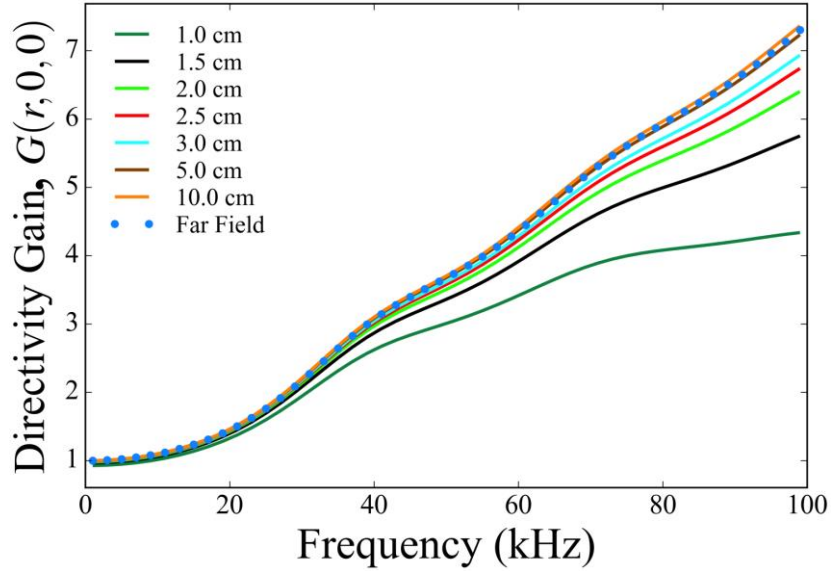


Figure S8. Dependence of the directivity gain function on frequency. Solid lines represent directivity gain $G(r,0,0)$ for different sphere radius calculated using Eq. S21 and Huygens-Fresnel principle. Dots line is a far field calculation of directivity gain $G(r, 0, 0)$ performed in accordance with Eq. S23

S2.6 COMSOL modeling

In order to confirm the theoretical approach based on the application of Eqs. S19 and S20 together with numerical Huygens-Fresnel calculation of the directivity gain function, we modeled our system using the COMSOL software. In our modeling, we used the acoustics module of COMSOL in a spherical region of space with the radius of 3 cm, which had a

bordering layer where we applied the “perfectly matched layer” routine. Within the above spherical region, we had a smaller rectangular region of sizes 1.25 cm x 1.25 cm x 0.2 cm which contained a square emitter of size 1 cm x 1 cm. In this rectangular region the acoustic module implemented thermoviscous acoustic simulations of the linearized Navier-Stokes equation, while in the entire spherical region it implemented acoustic pressure simulations using Helmholtz equations. Input for the simulations included temperature oscillation on the surface of $1 \times 1 \text{ cm}^2$ described by Eq. S7. The sketch of the overall simulation is shown in Figure S9.

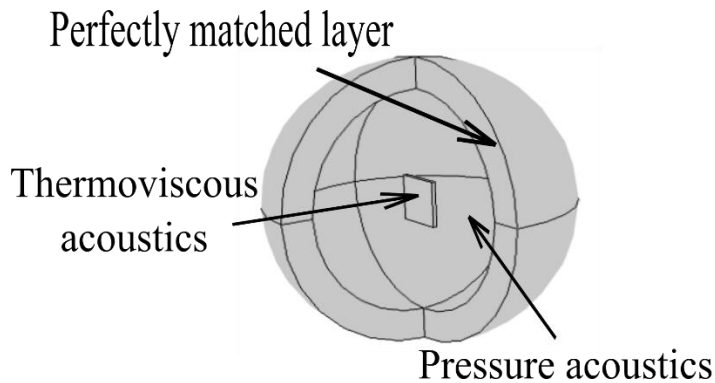


Figure S9. The principal geometry of the COMSOL modeling, including thermoviscous acoustic module, pressure acoustic module and perfectly matched layer.

The discretization mesh had at least 30 finite elements per wavelength, which led to significant calculation complexity at high frequencies. To overcome this problem, we used symmetric boundary conditions and directly modeled one-fourth of the space shown in the Figure S9. In the simulations we used the generalized minimal residual (GMRES) method with the parallel direct sparse solver (PARDISO) as a direct preconditioner.

References:

- (1) Aliev, A. E.; Gartstein, Y. N.; Baughman, R. H. Increasing the Efficiency of Thermoacoustic Carbon Nanotube Sound Projectors. *Nanotechnology* **2013**, *24* (23).

